Design of antireflective nanostructures and optical coatings for next-generation multijunction photovoltaic devices

Emmett E. Perl,[1,*] William E. McMahon,[2] John E. Bowers,[1] and Daniel J. Friedman[2]

[1]*Department of Electrical and Computer Engineering, University of California, Santa Barbara, CA, 93106, USA*
[2]*Concentrated Photovoltaics Group, National Renewable Energy Laboratory, Golden, CO, 80401, USA*
[*]*emmettperl@ece.ucsb.edu*

Abstract: The successful development of multijunction photovoltaic devices with four or more subcells has placed additional importance on the design of high-quality broadband antireflection coatings. Antireflective nanostructures have shown promise for reducing reflection loss compared to the best thin-film interference coatings. However, material constraints make nanostructures difficult to integrate without introducing additional absorption or electrical losses. In this work, we compare the performance of various nanostructure configurations with that of an optimized multilayer antireflection coating. Transmission into a four-junction solar cell is computed for each antireflective design, and the corresponding cell efficiency is calculated. We find that the best performance is achieved with a hybrid configuration that combines nanostructures with a multilayer thin-film optical coating. This approach increases transmitted power into the top subcell by 1.3% over an optimal thin-film coating, corresponding to an increase of approximately 0.8% in the modeled cell efficiency.

References and links

1. D. C. Law, R. R. King, H. Yoon, M. J. Archer, A. Boca, C. M. Fetzer, S. Mesropian, T. Isshiki, M. Haddad, K. M. Edmondson, D. Bhusari, J. Yen, R. A. Sherif, H. A. Atwater, and N. H. Karam, "Future technology pathways of terrestrial III–V multijunction solar cells for concentrator photovoltaic systems," Sol. Energy Mater. Sol. Cells **94**(8), 1314–1318 (2010).
2. R. R. King, A. Boca, W. Hong, X. Q. Liu, D. Bhusari, D. Larrabee, K. M. Edmondson, D. C. Law, C. M. Fetzer, S. Mesropian, and N. H. Karam, "Band-gap-engineered architectures for high-efficiency multijunction concentrator solar cells," in *24th European Photovoltaic Solar Energy Conference and Exhibition* 21, (2009).
3. F. Dimroth, M. Grave, P. Beutel, U. Fiedeler, C. Karcher, T. N. D. Tibbits, E. Oliva, G. Siefer, M. Schachtner, A. Wekkeli, A. W. Bett, R. Krause, M. Piccin, N. Blanc, C. Drazek, E. Guiot, B. Ghyselen, T. Salvetat, A. Tauzin, T. Signamarcheix, A. Dobrich, T. Hannappel, and K. Schwarzburg, "Wafer bonded four-junction GaInP/GaAs//GaInAsP/GaInAs concentrator solar cells with 44.7% efficiency," Prog. Photovolt. Res. Appl. **22**(3), 277–282 (2014).
4. P. T. Chiu, D. C. Law, R. L. Woo, S. B. Singer, D. Bhusari, W. D. Hon, A. Zakaria, J. Boisvert, S. Mesropian, R. R. King, and N. H. Karam, "Direct semiconductor bonded 5J cell for space and terrestrial applications," IEEE J. Photovoltaics **4**(1), 493–497 (2014).
5. P. Patel, D. Aiken, D. Chumney, A. Cornfeld, Y. Lin, C. Mackos, J. McCarty, N. Miller, P. Sharps, and M. Stan, "Initial results of the monolithically grown six-junction inverted metamorphic multi-junction solar cell," in *Proc 38th IEEE Photovoltaic Spec. Conf.*, (Institute of Electrical and Electronics Engineers, 2012), **vol. 2**, pp. 1–4.
6. R. M. France, I. Garcia, W. E. McMahon, A. G. Norman, J. Simon, J. F. Geisz, D. J. Friedman, and M. J. Romero, "Lattice-mismatched 0.7-eV GaInAs solar cells grown on GaAs using GaInP compositionally graded buffers," IEEE J. Photovoltaics **4**(1), 190–195 (2014).
7. D. J. Friedman, J. F. Geisz, A. G. Norman, M. W. Wanlass, and S. R. Kurtz, "0.7-eV GaInAs junction for a GaInP/GaAs/GaInas(1eV)/GaInAs(0.7eV) four-junction solar cell," in *Proc. 4th IEEE World Conference for Photovoltaic Energy Conversion*, (Institute of Electrical and Electronics Engineers, 2006), pp. 598–602.

8. M. A. Green, K. Emery, Y. Hishikawa, W. Warta, and E. D. Dunlop, "Solar cell efficiency tables (version 43)," Prog. Photovolt. Res. Appl. **22**(1), 1–9 (2014).
9. R. M. France, J. F. Geisz, M. A. Steiner, D. J. Friedman, J. S. Ward, J. M. Olson, W. Olavarria, M. Young, and A. Duda, "Pushing inverted metamorphic multijunction solar cells toward higher efficiency at realistic operating conditions," IEEE J. Photovoltaics **3**(2), 893–898 (2013).
10. J. F. Geisz, D. J. Friedman, J. S. Ward, A. Duda, W. J. Olavarria, T. E. Moriarty, J. T. Kiehl, M. J. Romero, A. G. Norman, and K. M. Jones, "40.8% efficient inverted triple-junction solar cell with two independently metamorphic junctions," Appl. Phys. Lett. **93**(12), 123505 (2008).
11. D. J. Friedman, J. M. Olson, and S. R. Kurtz, "High-efficiency III-V multijunction solar cells," in *Handbook of Photovoltaic Science and Engineering, 2nd Ed.*, A. Luque and S. Hegedus, eds, (Wiley, Chichester UK, 2011), 314–364.
12. D. J. Aiken, "High performance anti-reflection coatings for broadband multi-junction solar cells," Sol. Energy Mater. Sol. Cells **64**(4), 393–404 (2000).
13. W. H. Southwell, "Coating design using very thin high- and low-index layers," Appl. Opt. **24**(4), 457–460 (1985).
14. C. G. Bernhard, "Structural and functional adaptation in a visual system," Endeavor **26**, 79–84 (1967).
15. S. J. Wilson and M. C. Hutley, "The optical properties of moth eye antireflection surfaces," J. Mod. Opt. **29**, 993–1009 (1982).
16. H. A. Macleod, *Thin-Film Optical Filters* (CRC Press, Boca Raton, Fla., 2001), Chap. 4.
17. J. Tommila, A. Aho, A. Tukiainen, V. Polojärvi, J. Salmi, T. Niemi, and M. Guina, "Moth-eye antireflection coating fabricated by nanoimprint lithography on 1 eV dilute nitride solar cell," Prog. Photovolt. Res. Appl. **21**, 1158–1162 (2013).
18. D. Liang, Y. Kang, Y. Huo, Y. Chen, Y. Cui, and J. S. Harris, "High-efficiency nanostructured window GaAs solar cells," Nano Lett. **13**(10), 4850–4856 (2013).
19. J. Tommila, V. Polojärvi, A. Aho, A. Tukiainen, J. Viheriälä, J. Salmi, A. Schramm, J. M. Kontio, A. Turtiainen, T. Niemi, and M. Guina, "Nanostructured broadband antireflection coatings on AlInP fabricated by nanoimprint lithography," Sol. Energy Mater. Sol. Cells **94**(10), 1845–1848 (2010).
20. K.-H. Hung, T.-G. Chen, T.-T. Yang, P. Yu, C.-Y. Hong, Y.-R. Wu, and G.-C. Chi, "Antireflective scheme for InGaP/InGaAs/Ge triple junction solar cells based on TiO2 biomimetic structures," in *Proc 38th IEEE Photovoltaic Spec. Conf.*, (Institute of Electrical and Electronics Engineers, 2012), pp. 003322–003324.
21. P. Yu, M.-Y. Chiu, C.-H. Chang, C.-Y. Hong, Y.-L. Tsai, H.-V. Han, and Y.-R. Wu, "Towards high-efficiency multi-junction solar cells with biologically inspired nanosurfaces," Prog. Photovolt. Res. Appl. **22**(3), 300–307 (2014).
22. E. E. Perl, C.-T. Lin, W. E. McMahon, D. J. Friedman, and J. E. Bowers, "Ultra-broadband & wide-angle hybrid antireflection coatings with nanostructures," IEEE J. Photovoltaics **4**(3), 962–967 (2014).
23. J. Zhu, C.-M. Hsu, Z. Yu, S. Fan, and Y. Cui, "Nanodome solar cells with efficient light management and self-cleaning," Nano Lett. **10**(6), 1979–1984 (2010).
24. M. Victoria, C. Domínguez, I. Antón, and G. Sala, "Antireflective coatings for multijunction solar cells under wide-angle ray bundles," Opt. Express **20**(7), 8136–8147 (2012).
25. P. I. Stavroulakis, S. A. Boden, T. Johnson, and D. M. Bagnall, "Suppression of backscattered diffraction from sub-wavelength 'moth-eye' arrays," Opt. Express **21**(1), 1–11 (2013).
26. M. C. Hutley, "Diffraction gratings," in *Techniques of Physics*, (Academic Press, London, 1982).
27. D. G. Stavenga, S. Foletti, G. Palasantzas, and K. Arikawa, "Light on the moth-eye corneal nipple array of butterflies," Proc. Biol. Sci. **273**(1587), 661–667 (2006).
28. A. Garahan, L. Pilon, J. Yin, and I. Saxena, "Effective optical properties of absorbing nanoporous and nanocomposite thin films," J. Appl. Phys. **101**(1), 014320 (2007).
29. W. H. Southwell, "Gradient-index antireflection coatings," Opt. Lett. **8**(11), 584–586 (1983).
30. Y. M. Song, H. J. Choi, J. S. Yu, and Y. T. Lee, "Design of highly transparent glasses with broadband antireflective subwavelength structures," Opt. Express **18**(12), 13063–13071 (2010).
31. G. C. Park, Y. M. Song, E. K. Kang, and Y. T. Lee, "Size-dependent optical behavior of disordered nanostructures on glass substrates," Appl. Opt. **51**(24), 5890–5896 (2012).
32. W. E. McMahon, C.-T. Lin, J. S. Ward, J. F. Geisz, M. W. Wanlass, J. J. Carapella, W. Olavarría, M. Young, M. A. Steiner, R. M. France, A. E. Kibbler, A. Duda, J. M. Olson, E. E. Perl, D. J. Friedman, and J. E. Bowers, "Metal pillar interconnection topology for bonded two-terminal multijunction III-V solar cells," IEEE J. Photovoltics **2**, 868–872 (2013).
33. M. N. Polyanskiy, "Refractive Index Database" (2014), *http://refractiveindex.info*.
34. W. Shockley and H. J. Queisser, "Detailed balance limit of efficiency of p-n junction solar cells," J. Appl. Phys. **32**(3), 510–519 (1961).

1. Introduction

Multi-junction solar cells have achieved the highest efficiencies of all photovoltaic technologies. Today, triple-junction (3-J) cells are the industry standard for concentrated photovoltaic and space photovoltaic systems. However, the field is rapidly moving towards

designs that incorporate additional junctions in order to achieve higher power conversion efficiencies [1–7]. Recently, world record efficiencies of 44.7% at 297-suns and 38.8% at 1-sun have been reported using designs with four and five junctions respectively [3,8].

These four-junction (4-J) and five-junction (5-J) designs absorb light across a very broad wavelength range (~300-1800 nm) and have strict current matching requirements for each of the subcells [1–4]. The broadband performance of the antireflection coating (ARC) is thus more critical for these designs than for today's best 3-J devices, which incorporate either a germanium bottom junction that is oversupplied with photons and can better tolerate high infrared reflectivity or a bottom junction with a bandgap around 1.0 eV and a narrower absorption range (~300-1250 nm) [9–12].

There are several approaches to improving the broadband performance of the ARC. Step-down interference coatings consisting of three or more layers can improve upon today's standard two-layer coatings. Similar quality can be obtained using structures with alternating layers of high- and low-index materials [12,13].

Antireflective nanostructures have been proposed as an alternative to interference based ARCs. These designs consist of sub-wavelength structures that act to provide a gradient in the effective index of refraction from air to the top semiconductor layer. By eliminating abrupt steps in the refractive index, Fresnel reflections are greatly reduced [14,15].

Ideally, the nanostructures would not absorb a significant amount of incoming light and would be composed of a material with a refractive index similar to the top layer of the device [11]. Unfortunately, it is difficult to find suitable materials with a low extinction coefficient and high refractive index across the solar spectrum [16]. This leads to a design tradeoff between material absorption for nanostructures composed of commonly available high-index materials and increased Fresnel reflections at the interface between the nanostructured layer and the uppermost III-V layer for nanostructures composed of commonly available low-absorption materials.
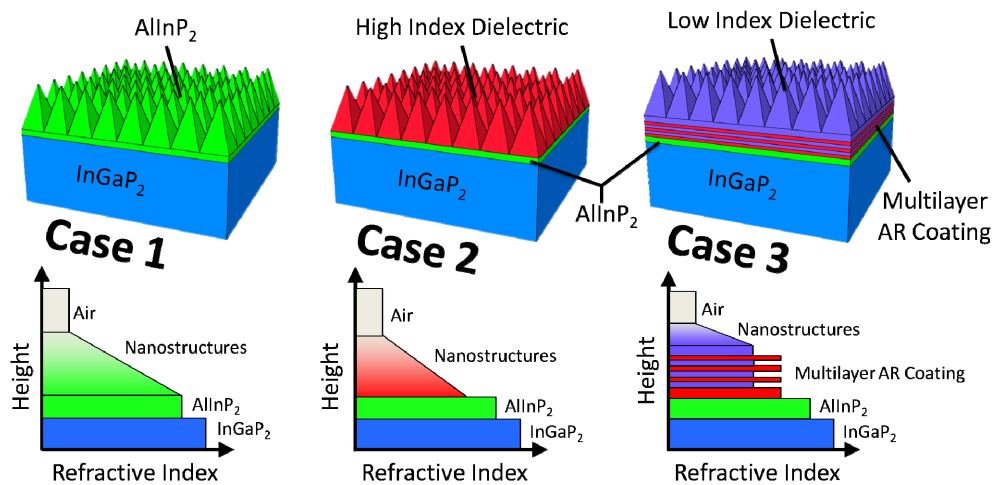

Fig. 1. Diagram of the antireflective nanostructure designs explored in this paper. The top semiconductor layers are composed of a ~1 μm thick layer of indium gallium phosphide (InGaP$_2$) and a ~20 nm thick layer of aluminum indium phosphide (AlInP$_2$).

In this work, we explore this tradeoff by examining the performance of various antireflective nanostructure designs by modeling reflection, absorption, transmission, and cell efficiency for a 4-J solar cell. For Case 1, we look at the configuration where the uppermost aluminum indium phosphide (AlInP$_2$) "window" layer is thickened and patterned with nanostructures [17–19]. For Case 2, we look at the configuration where the nanostructures are placed into a low-absorption, high-index dielectric layer [20,21]. For Case 3, we look at the

hybrid configuration where a nanostructured layer is integrated on top of an interference based ARC [22]. These three configurations are shown in Fig. 1.

The performance of each design is evaluated as the height of the nanostructures is varied from 0 to 1000 nm. The limiting case for where the nanostructure height is zero corresponds to a design with no ARC for Cases 1 and 2 and a design with a multilayer ARC for Case 3.

In order for these designs to translate to an improvement in cell efficiency, it is essential that they have minimal absorption and electrical loss. Direct patterning of the solar cell alters the electrical properties of the device, often leading to a reduction in fill factor and open circuit voltage [18,23]. Here, we consider only antireflective designs that do not require the electrically active layers of the device to be changed. Thus, absorption and reflection are the dominant sources of loss for these structures, and the quality of the design can be closely coupled to the power transmitted into the top junction of the solar cell. The primary focus of this work is to provide design guidance for the integration of broadband antireflective nanostructures and optical coatings with multijunction photovoltaics.

2. Optical design for broadband antireflection

The high refractive index of the III-V materials used in multijunction solar cells leads to a power loss of roughly 30% at the top interface of the device due to Fresnel reflection. If these losses are not minimized using antireflection coatings or nanostructures, they will translate directly to a significant reduction in cell efficiency. Reflection losses can be greatly reduced by depositing a multilayer thin-film ARC on top of the photovoltaic device or by fabricating nanostructures that produce a gradient in the effective refractive index of the material.

2.1 Design rules for a multilayer ARC

Figure 2 shows the reflectance spectrum for a single-layer optical coating placed on a hypothetical substrate with a refractive index of four.
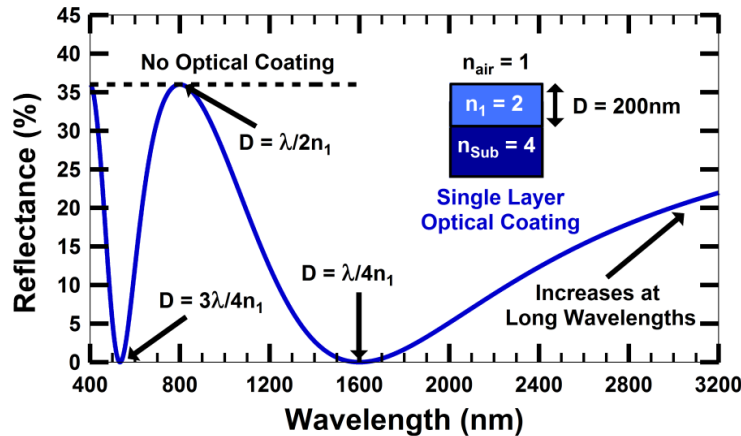

Fig. 2. Plot showing the reflectance spectrum for a single layer optical coating with visible maxima at $D = \lambda/2n_1$ and minima at $D = \lambda/4n_1$ and $3\lambda/4n_1$.

Perfect antireflection is achieved when two conditions are met. First, the partial reflections from the front and back interface of the thin-film layer must be 180° out of phase leading to destructive interference between the first reflection and all subsequent partial reflections. This condition is satisfied when the thickness of the thin-film layer is equal to $\lambda/4n_1 + m\lambda/2n_1$ ($m = 0,1,2\ldots$), where λ is the wavelength of incoming light and n_1 is the refractive index of the thin-film layer. Second, the magnitude of the front reflection must be equal to the magnitude of the sum of all other partial reflections in the thin-film layer. This condition is

met when the refractive index of the thin-film layer is the geometric mean of the refractive indices of its surrounding layers: $n_1 = \sqrt{n_{air} n_{Sub}}$ [16].

The widest band of low reflection occurs at the $\lambda/4n_1$ minimum. However, the region of low reflectivity for a single-layer optical coating cannot adequately cover the entire absorption width of a multi-junction solar cell [12].

To increase the width of the low reflectivity region, additional thin-film layers can be deposited to make it a multilayer ARC. Similar to a single-layer ARC, optimal performance is obtained when the refractive index of each layer is the geometric mean of the refractive indices of its two neighboring layers. Each layer has the effect of adding a minimum to the reflectance spectrum, which can be used to increase the width of the low reflectivity region. Ideal step-down interference coatings with three or more layers can greatly reduce reflection across most of the solar spectrum [12,24].

Figure 3 shows the refractive index and extinction coefficient for common materials used in the design of antireflection coatings for multijunction solar cells. The top of a multijunction device will commonly consist of a thick (~1 μm) layer of indium gallium phosphide ($InGaP_2$) topped with a thin (~10-20 nm) layer made of $AlInP_2$ [11]. Both of these materials are lattice matched to gallium arsenide (GaAs). Titanium dioxide (TiO_2), tantalum pentoxide (Ta_2O_5), and silicon dioxide (SiO_2) are regularly used for thin-film optical coatings. Few materials exist with a refractive index lower than SiO_2 (n ≈1.5) or with an absorption edge below 400 nm and a refractive index higher than TiO_2 (n ≈2.4). The refractive indices of these materials are therefore representative of the lower and upper bounds for low-absorption materials that can be used in solar cell ARC design [16].
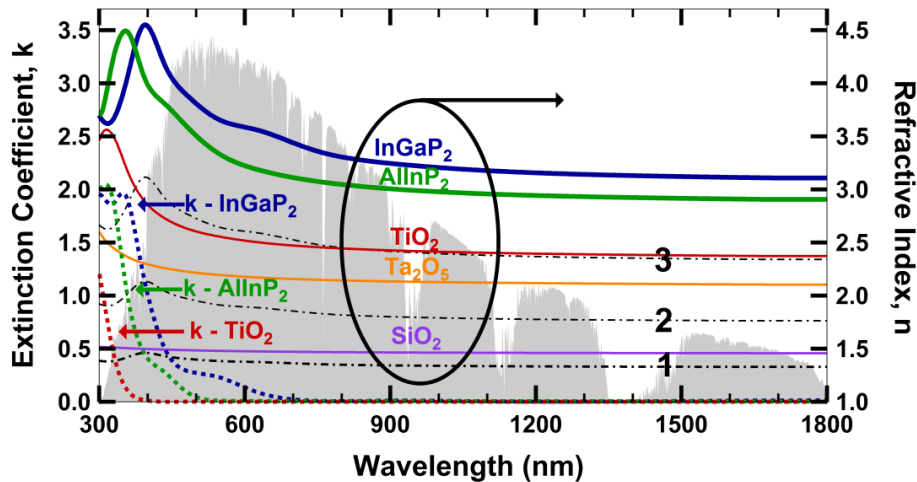

Fig. 3. Plot showing the refractive index (solid lines) and extinction coefficient (dashed lines) for the top two layers of a typical multijunction cell ($InGaP_2$ and $AlInP_2$) and common materials used for thin-film antireflection coatings (TiO_2, Ta_2O_5, and SiO_2). The dash-dotted black lines show the ideal refractive indices for a 3-layer step-down interference coating.

The three dash-dotted black lines represent the ideal indices of refraction for a 3-layer step-down interference coating for $InGaP_2$. In practice, it is often difficult to find intermediate-index materials with refractive indices that are close to ideal. To circumvent this problem, it is possible to obtain the equivalent optical properties of an intermediate-index layer with a stack consisting of alternating layers of high- and low-index materials [12,13].

Since these multilayer designs quickly become complex and difficult to analyze, we optimize the layer thicknesses by minimizing a merit function that describes the quality of the coating. Equation (1) shows the merit function used to optimize all of the thin-film coating designs in this study.

$$F = \int_{\lambda_{\min}}^{\lambda_{\max}} P(\lambda)*[1-T(\lambda)]d\lambda. \tag{1}$$

λ_{min} and λ_{max} represent the short and long wavelength cutoffs of the device, $P(\lambda)$ is a weighting function describing the power in the AM1.5D spectrum, and $T(\lambda)$ is the transmittance computed using the transfer-matrix method. For our designs, we choose λ_{min} to be 300 nm and λ_{max} to be 1675 nm, corresponding to a 4-J design with a 0.73 eV $In_{0.53}Ga_{0.47}As$ bottom junction grown lattice-matched to InP.

While the layer structure of a 4-J photovoltaic device can vary depending on its design and on the growth conditions, the top two layers typically do not change significantly. For this reason, transmittance is calculated into the top junction only. By minimizing the merit function, transmitted power is maximized through the 20 nm $AlInP_2$ window layer and into the $InGaP_2$ top junction. Since the underlying layers are typically composed of III-V materials with a refractive index similar to that of $InGaP_2$, we find that there is not a significant difference in the design of an ARC that is optimized using a more complex optical model.

For systems that have additional optical elements, such as a CPV module, the merit function can be modified to more accurately describe the optical system. Losses from a primary or secondary concentrating optic can be taken into account by modifying $P(\lambda)$ to describe the attenuated spectrum that will ultimately reach the front end of the photovoltaic device. Additionally, the angular characteristics of a CPV module could be considered by modifying $P(\lambda)$ to $P(\lambda,\theta)$ and $T(\lambda)$ to $T(\lambda,\theta)$, then integrating across the angular range of the concentrating system.

2.2 Design rules for antireflective nanostructures

Antireflective nanostructures have been proposed as an alternative to multilayer ARCs, and have demonstrated excellent broadband and wide-angle antireflective properties. These surfaces consist of a regular array of protrusions where the areal fraction of air to the nanostructure material is smoothly increasing with height. If the lateral spacing between adjacent features is less than the wavelength of light, incoming photons will see a gradient in the effective index of refraction throughout the nanostructured layer. This tapered profile and index gradient is illustrated in Fig. 1 [14,15].

The lateral spacing, height, shape, refractive index, and absorption coefficient of the nanostructures are critical to the antireflective properties of the system. If the spacing between features is greater than the wavelength of incoming light, the surface will scatter or diffract incident photons and may not have the desired optical properties. For a perfectly periodic array, the nanostructure surface would act as a diffraction grating where transmitted light is diffracted to an angle determined by Eq. (2).

$$\sin(\theta_T) = \frac{m\lambda_0}{nd} + \sin(\theta_I). \tag{2}$$

Where θ_T is the transmission angle for the diffracted beam, m is the diffraction order ($m = 0, \pm 1, \pm 2,...$), λ_0 is the wavelength of light in vacuum, n is the refractive index of the nanostructure material, d is the lateral spacing between nanostructures, and θ_I is the angle of incidence for incoming light [25,26].

For the case where $\lambda/(2n*d) > 1$, only zero[th] order diffraction is possible for all angles of incidence. In this case, $\theta_T = \theta_I$, and all incoming light will see the nanostructured layer as an effective medium with a smoothly varying refractive index. In order to suppress all higher diffraction orders, it is necessary that the spacing between features be smaller for structures

placed into high-index materials than for structures placed into low-index materials. The relative spacing required for nanostructures placed into AlInP$_2$ and SiO$_2$ is shown in Eq. (3).

$$\frac{d_{AlInP_2}}{d_{SiO_2}} = \frac{d_{SiO_2}}{d_{AlInP_2}} \approx \frac{1}{2}.$$ (3)

In order to calculate the optical properties of the surface, it is necessary to develop a model for the nanostructures. Since the effective index of refraction will change as light moves through the structure, partial reflections will arise at every depth in the surface. The net reflectance can be found by considering the sum of all partial reflections, each having a different phase that is dependent on the distance travelled through the structure. For nanostructure heights greater than $\lambda/2$, all phases are present in the reflected beam and destructive interference will cause the net reflectance to approach zero [15].

The surface can be approximated by splitting the nanostructures into a large number of evenly spaced thin horizontal slices, where the effective index of refraction and extinction coefficient for each layer is calculated using volume averaging theory [27,28]. Reflectance, absorptance, and transmittance can then be modeled using the transfer-matrix method.

The number of layers must be chosen such that the spacing between adjacent slices is much smaller than the wavelength of incoming light. The ratio of the layer spacing to the wavelength of light is shown in Eq. (4).

$$\frac{S}{\lambda} = \frac{H*n}{\lambda_0 * (\# \ of \ slices)}.$$ (4)

Where S is the spacing between slices, λ is the wavelength of light in the layer, H is the height of the nanostructures, n is the effective index of refraction in the slice, and λ_0 is the wavelength of light in vacuum. When modeling tall nanostructures composed of a material with a high index of refraction, a larger number of slices are required to keep this ratio constant. In this study, the tallest nanostructures considered have a height of 1000 nm and the nanostructures with the largest refractive index are composed of AlInP$_2$.

Figure 4 shows the calculated reflectance spectrum for 1000 nm tall AlInP$_2$ nanostructures placed on top of an AlInP$_2$ substrate. The different lines show how the calculation varies as the number of slices used to approximate the structures change.
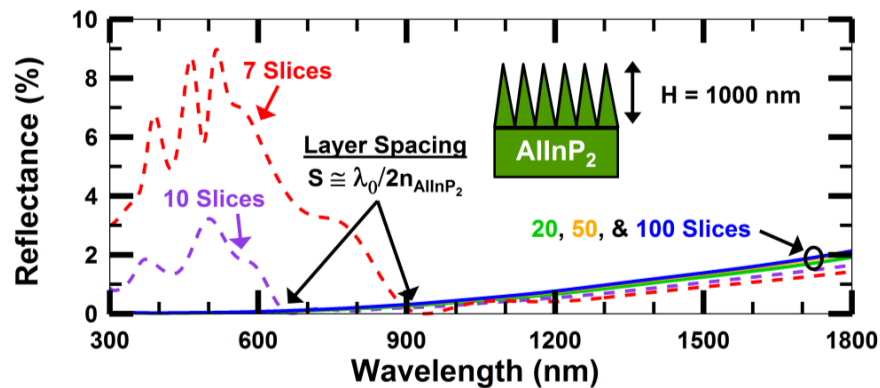

Fig. 4. Plot showing the reflectance spectrum for 1000 nm tall AlInP$_2$ nanostructures. The calculation begins to converge when the number of slices is greater than 20.

It is evident from Fig. 4 that the accuracy of the model breaks down when the number of slices used in the model is too small. This is visible at short wavelengths, where a significant deviation in the calculated reflectance occurs when the layer spacing is larger than

$\lambda_0/2n_{AlInP2}$. In order to accurately model the nanostructures, it is necessary that the spacing between adjacent slices is less than this for the shortest wavelength considered.

As the number of slices used to approximate the nanostructures increases, the calculation begins to converge. For $S < \lambda_0/5n_{AlInP2}$, we find that the deviation in the modeled reflectance becomes linearly dependent on the spacing between slices. For approximations which use 50, 100, and an infinite number of slices, the layer spacing will decrease from 20 nm to 10 nm to 0 nm. This means that the deviation in the calculated reflectance for models using 50 and 100 slices will be equivalent to the deviation for models using 100 and infinite number of slices. For 300-1800 nm light, we find that the average calculation error is just 0.02% for the 100 slice model. For smaller nanostructure heights and for structures composed of lower index materials, this deviation is expected to be even smaller since the ratio of S/λ will decrease. For all further calculations in this paper, the nanostructures will be approximated using a 100 slice model.

Using this model, we find that the optical properties of the surface are highly dependent on the nanostructure height. Figure 5 shows the effect of nanostructure height on the reflectance spectrum for SiO_2 nanostructures placed on top of a SiO_2 substrate and $AlInP_2$ nanostructures placed on top of an $AlInP_2$ substrate. The lateral dimensions are assumed to be small enough that no diffraction or scattering occurs throughout the entire wavelength range.
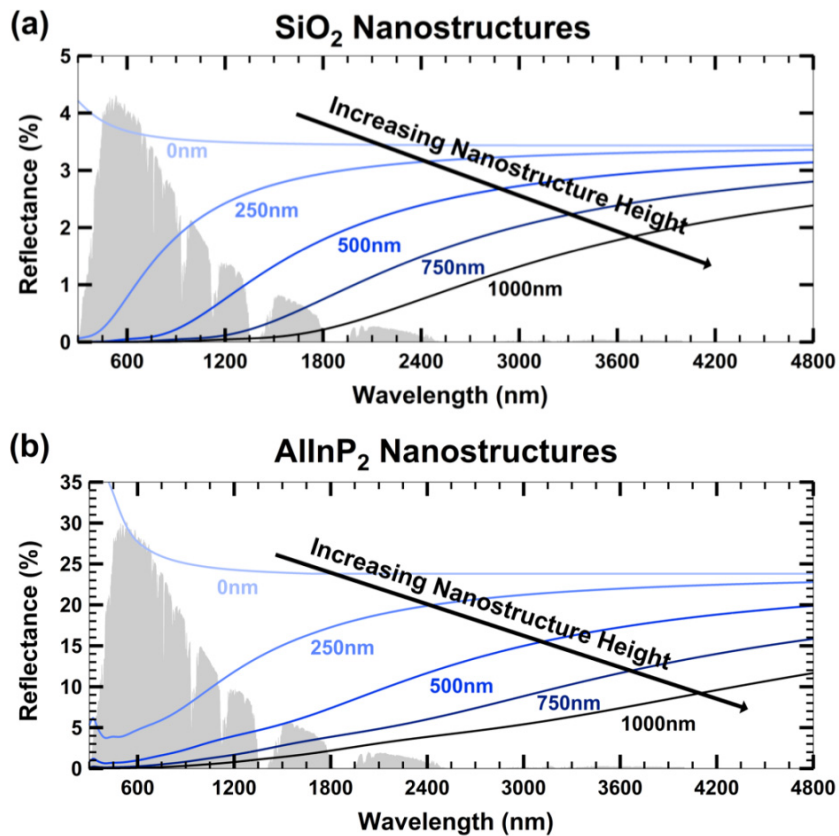

Fig. 5. Plots showing reflectance as a function of wavelength for (a) SiO_2 nanostructures placed on top of a SiO_2 substrate and (b) $AlInP_2$ nanostructures placed on top of an $AlInP_2$ substrate. The nanostructure height is varied from 0 to 1000 nm.

For these calculations, the nanostructures are assumed to have a quintic index profile, which has been shown to be very close to ideal for a graded-index antireflection coating [29].

The reflective properties of nanostructures with different shape profiles have been theoretically explored in detail elsewhere [29–31].

In the limit where the wavelength is much larger than the nanostructure height, reflectance approaches that of the Fresnel reflection at a sharp interface. This acts as the upper bound for reflectance in the nanostructured layer. In Fig. 5, this effect is illustrated at very long wavelengths for the case where the nanostructure height is 250 nm. This upper bound is larger for structures composed of high-index materials such as $AlInP_2$ than for structures composed of low-index materials such as SiO_2.

When designing for 4-J or 5-J solar cell operation, it is important to minimize reflection for light with wavelengths between 300 and 1800 nm. The height of the nanostructures must be chosen to ensure that the region of low reflectivity matches the absorption range of the device. For $AlInP_2$, which is index matched to the top layer of the device, the nanostructure height would need to be around 1000 nm to adequately reduce reflection below that of an optimal multilayer ARC.

It is also important to consider absorption in the nanostructured layer. Figure 3 shows the extinction coefficient of $AlInP_2$, and suggests that absorption will be significant at short wavelengths if the nanostructure height must be around 1000 nm. This is also true for most materials with a refractive index similar to the uppermost III-V layers of a solar cell. TiO_2 and ZnS represent the highest index materials that will not absorb a significant amount of light in the solar spectrum [16].

2.3 Design parameters for nanostructure configurations

It is clear that material selection is critical for the integration of antireflective nanostructures with multijunction solar cells. The refractive index and extinction coefficient of the material has a significant effect on absorption, scattering, and reflection losses.

We model the performance of the three proposed nanostructure configurations shown in Fig. 1 as the height of the nanostructures is varied from 0 to 1000 nm. For Case 1, the nanostructures are composed of $AlInP_2$, which is index matched to the top layer of the multijunction cell. For Case 2, the nanostructures are composed of low-absorption, high-index dielectric materials; SiO_2, GaP, Ta_2O_5, TiO_2, and ZnS are considered. For Case 3, we consider a hybrid configuration where antireflective nanostructures are placed into SiO_2, a low-index dielectric, which is placed on top of a multilayer ARC designed for maximum transmission into the solar cell. An optimized multilayer ARC and no ARC are also considered as limiting cases for when the nanostructure height is zero.

The optical stack modeled is a 4-J bonded solar cell with a 1.85 eV $InGaP_2$ top junction, a 1.42 eV GaAs 2nd junction, a 1.05 eV indium gallium arsenide phosphide (InGaAsP) 3rd junction, and a 0.74 eV indium gallium arsenide (InGaAs) bottom junction. There is a 20-nm thick $AlInP_2$ layer on top of the $InGaP_2$ junction to passivate the surface [3,32]. All of the optical constants used in the model are reported in the Sopra optical database or measured using spectral ellipsometry [33].

The layer thicknesses for the thin-film ARC in Case 3 are found by first performing a global search, then using a simplex optimization to minimize the merit function described in Eq. (1) [22]. The optimization accounts for absorption and reflection in the thin $AlInP_2$ layer, which is important when designing an ARC for a real solar cell. The nanostructures are assumed to have a quintic index profile, and the layer thicknesses are reoptimized at each nanostructure height.

Designs with a single layer of TiO_2 and 4 alternating pairs of Ta_2O_5/SiO_2 are used as the starting point for the optimization. This design can have similar optical properties to a step-down interference coating with up to 6 layers. TiO_2 is representative of the thin-film material with the highest achievable refractive index, and is thus used as the layer adjacent to $AlInP_2$. The intermediate index layers are built up using alternating pairs of Ta_2O_5 and SiO_2, where a $Ta_2O_5/SiO_2/Ta_2O_5$ combination can approximate the optical properties of an intermediate

index layer. Ta_2O_5 is used instead of TiO_2 to help minimize absorption loss in the final structure [12,13].

It is important to note that the optimization process often reduces the number of layers. We use 9-layers as a starting point to get an upper limit on performance and to gain intuition for how the optimal multilayer design changes as the nanostructure height is varied. However, optimal performance can often be achieved using stacks with 2 or 3 alternating pairs of Ta_2O_5/SiO_2, making it possible to simplify the design and reduce costs.

Figure 6 shows the designs for the hybrid configuration of Case 3, where the cumulative height of the multilayer coating is plotted as a function of nanostructure height.
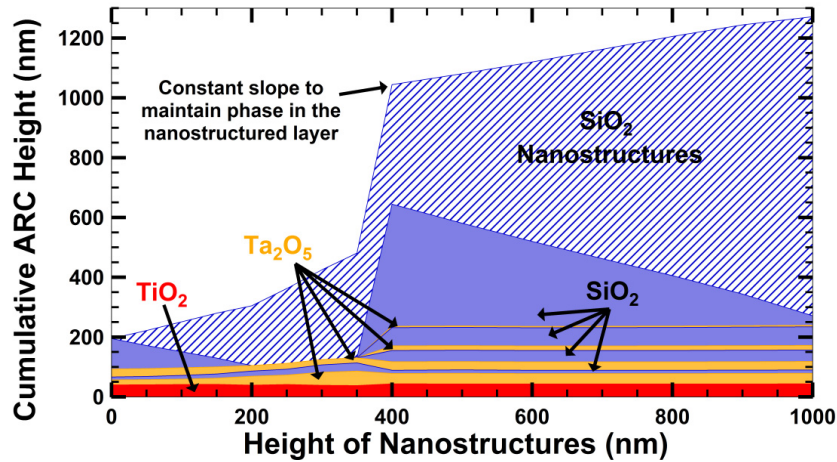

Fig. 6. Plot showing the cumulative height of the multilayer ARC for the hybrid configuration (Case 3) as a function of nanostructure height.

This plot has a lot of interesting features relevant to the optical design of the ARC. First, note that when the nanostructure height is less than 400 nm, the optimal number of layers collapses from nine to five. This behavior can be linked to the design of an ideal step-down interference coating.

The ideal indices of refraction for a three-layer step-down coating from air-$InGaP_2$ are shown in Fig. 3. Since the top and bottom layers have refractive indices very close to SiO_2 and TiO_2, only one intermediate index layer needs to be built up with a Ta_2O_5/SiO_2 equivalent stack. The ideal indices for a four-layer step-down interference coating would require materials with indices lower than SiO_2 and higher than TiO_2, which cannot be achieved using commonly available thin-film materials [12,16].

For nanostructure heights greater than 400 nm, the design of a step-down interference coating is better approximated by choosing ideal indices that bridge the gap between SiO_2 and $InGaP_2$. All intermediate layers with a refractive index lower than TiO_2 are obtainable, so a design consisting of more than five layers becomes ideal.

Another interesting feature from Fig. 6 is the dependence of the Ta_2O_5 and SiO_2 layer thicknesses on stack position. For designs with a nanostructure height greater than 400 nm, each Ta_2O_5 layer gets thinner and each SiO_2 layer gets thicker near the top of the stack. This translates to higher equivalent indices at the bottom of the stack and lower equivalent indices at the top of the stack. This trend illustrates how the alternating layers of Ta_2O_5 and SiO_2 build up a stack with similar properties to an ideal step-down interference coating.

Also note the decreasing thickness of the uppermost SiO_2 layer as the height of the nanostructures increases. This layer has the purpose of maintaining the phase shift for incoming light reflected off the first Ta_2O_5 layer. This results in a nearly constant slope in the

cumulative ARC height, and leads to comparable performance for all designs with a nanostructure height greater than 400 nm [15].

3. Results and discussion

The quality of each nanostructure design is evaluated by modeling reflection, absorption, transmission, and cell efficiency for a 4-J photovoltaic device. The model considers reflection and absorption loss in the full optical stack, assuming that absorption in the layers between each junction is negligible. A conventional multijunction cell model is used to calculate the cell efficiency of a 4-J device for each of the antireflective nanostructure designs [11].

3.1 Antireflective design comparisons

Figures 7(a)-7(c) show transmitted, absorbed, and reflected power for each configuration as the height of the nanostructures is varied. These values are expressed as percentages summing to 100%. For Case 2, only the results for TiO_2 are plotted. Transmission for SiO_2, GaP, ZnS, and Ta_2O_5 nanostructures was also calculated, but found to be lower than for TiO_2 nanostructures.
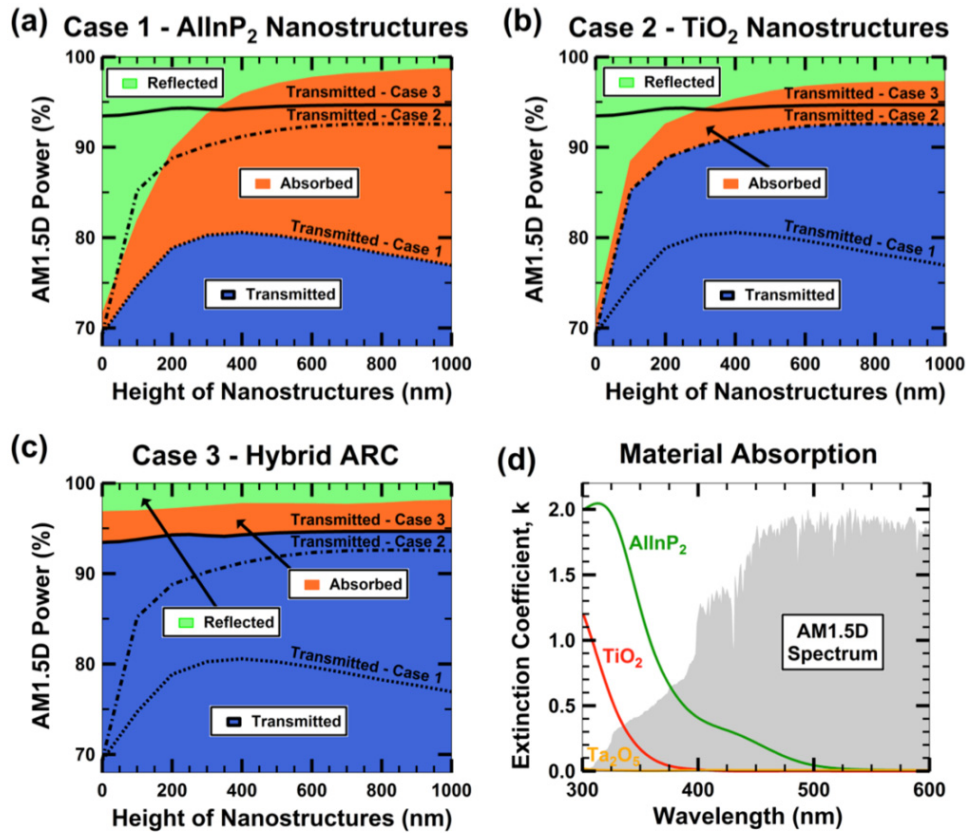

Fig. 7. Plots showing transmitted, absorbed, and reflected power for (a) Case 1 - $AlInP_2$ nanostructures, (b) Case 2 – TiO_2 nanostructures, (c) Case 3 – The hybrid ARC design. (d) Plot showing absorption for the materials used in the nanostructure designs.

These plots illustrate the tradeoff between absorption in the nanostructures and increased Fresnel reflection at the $AlInP_2$ window layer interface. Case 1 is limited by absorption, which increases rapidly as the nanostructures become tall due to the high extinction

coefficient of AlInP$_2$. Case 2 is limited by reflection due to index mismatch between TiO$_2$ and AlInP$_2$. Case 3 is the best performing design, achieving low absorption and low reflection.

Figure 7(d) shows material absorption for AlInP$_2$, TiO$_2$, and Ta$_2$O$_5$. Absorption loss is closely related to the extinction coefficient, k, and can be quantified using Eq. (5).

$$Absorption\ Loss = 1 - e^{(-4\pi kD/\lambda)}. \tag{5}$$

Where k is the extinction coefficient, D is the distance traveled through the material, and λ is the wavelength of light in vacuum. The optical model includes absorption loss in the 20 nm thick AlInP$_2$ window layer, which accounts for a power loss of 2-3% for all configurations.

Table 1 shows reflected power, absorbed power, and transmitted power for each case when the nanostructure height is optimal. For comparison, results from the multilayer ARC and no ARC are shown. The hybrid approach (Case 3) is the most effective antireflective nanostructure design and the only nanostructure design that outperforms an optimal multilayer ARC.

Table 1. Antireflection Coating Comparison

Configuration	Nanostructure Height	Reflected Power	Absorbed Power	Transmitted Power
No ARC	0 nm	28.4%	2.2%	69.4%
Multilayer ARC	0 nm	3.2%	3.4%	93.4%
Case 1 – AlInP$_2$	400 nm	4.1%	15.3%	80.6%
Case 2 – TiO$_2$	800 nm	2.8%	4.6%	92.6%
Case 3 – Hybrid	900 nm	1.8%	3.5%	94.7%

The hybrid ARC design increases transmitted power by 25.3% compared to no ARC, 14.1% compared to AlInP$_2$ nanostructures, 2.1% compared to TiO$_2$ nanostructures, and 1.3% compared to an optimal multilayer ARC. Additionally, scattering loss from the nanostructures is expected be lowest for the hybrid design since the features are placed into a low-index SiO$_2$.

Figure 8 shows AM1.5D power loss as a function of wavelength for each of the three cases. The box to the right shows the top subcell power loss for a top junction bandgap of 1.8 eV and 1.9 eV.
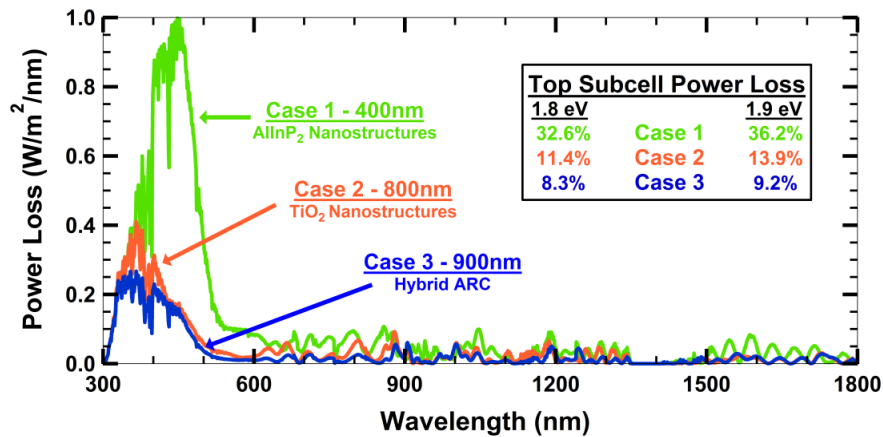

Fig. 8. Plots showing the sum of reflection and absorption losses as a function of wavelength for the best configuration from Cases 1, 2, and 3. The percentage of power lost in the top subcell is shown in the box on the top right of the plot.

The largest optical loss for each case occurs at short wavelengths, leading to a decrease in the power available to the top subcell. Absorption loss is most significant for the AlInP$_2$ nanostructures, which absorb a significant amount of light at wavelengths less than 500 nm. The TiO$_2$ nanostructures absorb light below 400 nm, and also have a higher reflectance than the hybrid design across most of the solar spectrum.

3.2 Cell efficiency model

Transmittance from the optimal design for each of the three cases is incorporated into a cell efficiency model [11]. Efficiency is calculated for two different top cell bandgaps (1.8 and 1.9 eV). In the model, the bandgaps for the second and third subcell are varied to maximize efficiency, and the bandgap of the bottom subcell is set at 0.74 eV. Some assumptions in the model include the conversion of all absorbed photons into photocurrent, a concentration of 1000 suns, and a temperature of 300 K. Junction dark currents are computed by the Shockley-Queisser method [34]. Subcell thinning is allowed when it is beneficial for the design [11].

Figure 9 shows the results from the cell efficiency model. We see that there is an excellent correlation between cell efficiency and power loss.
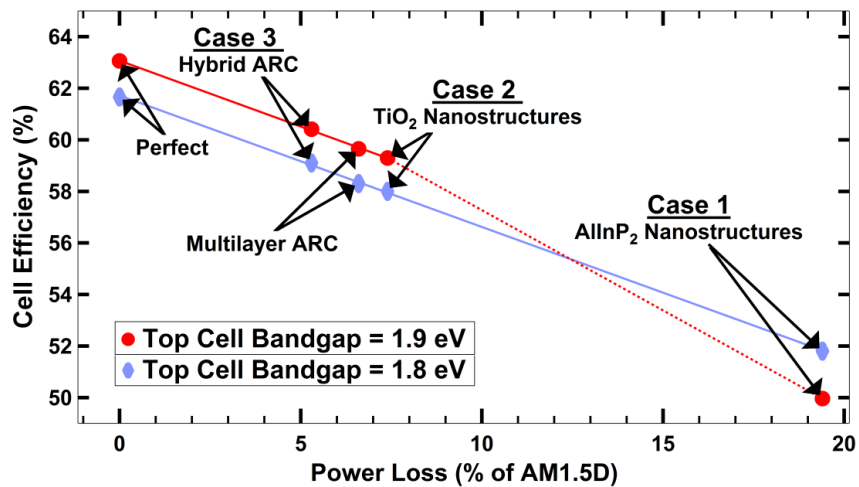

Fig. 9. Correlation between AM1.5D power loss and modeled cell efficiency at 1000 suns concentration. The two solid lines show linear fits to the data. The dashed line shows where the linear correlation between cell efficiency and power loss breaks down due to undersupply of photons to the top subcell.

The linear correlation between power loss and modeled cell efficiency can be explained by cell thinning. Typically, a top subcell composed of InGaP$_2$ is oversupplied with photons in a multijunction cell. As long as the top junction is oversupplied, it is possible to distribute light to the other junctions until optimal subcell currents are achieved. With cell thinning allowed, efficiency is linearly correlated with optical loss from the antireflective nanostructures.

When the AlInP$_2$ nanostructures are placed onto a cell with a 1.9 eV top junction bandgap, the top subcell becomes undersupplied with photons. The large efficiency drop observed for this case occurs as the top subcell becomes current limited to a value much lower than what is optimal for a 4-J configuration.

The absolute efficiencies from Fig. 9 represent an upper limit. While these efficiencies may not be possible to achieve, their relative values provide a metric to evaluate the quality of the optical design. Furthermore, the linear correlation between cell efficiency and power loss in the antireflective nanostructures indicates that an optical design that maximizes

transmission into the solar cell is near ideal when cell thinning can be used as a tool to optimize subcell currents.

4. Conclusion

In this work, we explore the design rules for the integration of broadband antireflective nanostructures and optical coatings with multijunction photovoltaics. Material selection is critical to the antireflective properties of any optical design. The primary challenge for integrating nanostructures with multijunction solar cells results from a lack of suitable materials with a low extinction coefficient and high refractive index, leading to an unavoidable tradeoff between material absorption for nanostructures made of common high-index materials and increased Fresnel reflection at the window layer interface for nanostructures made of common low-loss materials.

Absorption, scattering, and reflection losses are largest for nanostructures composed of materials with a refractive index similar to the uppermost III-V layers of a solar cell. These losses are reduced for nanostructures composed of high-index dielectric materials, but the lower refractive index of the nanostructures leads to the introduction of a Fresnel reflection at the $AlInP_2$ "window" layer interface. Nanostructures placed into low index materials, such as SiO_2, will have the lowest absorption, scattering, and reflection loss. However, for these designs, it is essential to incorporate a multilayer ARC to minimize the resulting Fresnel reflection from the $SiO_2/AlInP_2$ interface.

The performance of antireflective nanostructures composed of various high- and low-index materials is quantitatively compared by modeling reflectance, absorptance, transmittance, and cell efficiency for a bonded 4-J solar cell. The best performance is achieved with a hybrid design that combines a multilayer ARC with nanostructures placed into a low-index SiO_2 layer. This approach maintains low power reflection and low absorption across the solar spectrum, resulting in an increase of approximately 14.1% in transmitted power compared to nanostructures placed into $AlInP_2$, 2.1% compared to nanostructures placed into TiO_2, and 1.3% compared to an optimized multilayer ARC design. This corresponds to a 0.8% improvement in the modeled cell efficiency for a 4-J solar cell compared to a design with an optimal interference based ARC. The integration of antireflective SiO_2 nanostructures using a hybrid design should result in a direct improvement in cell efficiency for the next-generation of multijunction solar cells.

Acknowledgments